ChemPubSoc Europe

DOI: 10.1002/cssc.201901377

CHEMSUSCHEM Full Papers

Positive Surface Pseudocapacitive Behavior-Induced Fast and Large Li-ion Storage in Mesoporous $LiMnPO_4$@C Nanofibers

Hao Yang,[a] Jingyuan Liu,[b] Xiaofei Wang,[a] Chengcheng Zhao,[a] Lina Wang,*[a] Yonggang Wang,[b] Yongyao Xia,[b] and Tianxi Liu*[a]

Olivine-structured $LiMnPO_4$ (LMP) is an efficient Li^+ host owing to its high theoretical energy density and thermal stability. However, its poor ionic and electronic conductivity severely hinder its practical application. Herein, one-dimensional (1D) LMP@C nanofibers with in situ created 3D mesoporous architecture are reported and the charge-storage behavior is addressed. Ultrafine LMP nanoparticles are homogeneously confined in the nanofibers with interconnected and exposed mesoporous intersections, facilitating the electronic/ionic transportation and retarding the pulverization/fracture of electrodes. Remarkably, the hierarchical construction promotes a certain degree of pseudocapacitive contribution. The diffusion-controlled battery-type and surface-controlled capacitive faradaic redox processes act synergistically, giving new insights into Li-ion storage cathode materials to reach the common goal of high energy density and power density simultaneously. The current separation technique suggests surface-dominated pseudocapacitance as the major Li^+ storage mechanism at high rates, which is regarded as an efficient way to improve the rate performance. Hence, the as-prepared LMP@C nanofibers could deliver a high reversible capacity of 149.8 mAh g^{-1} with 92% charge retention over 300 cycles at 0.2 C (1 C = 171 mA g^{-1}). Even at a high rate of 5 C, a capacity of 63.1 mAh g^{-1} is retained after 2000 cycles with an exceptional cyclic stability.

Introduction

Lithium-ion batteries remain the dominant power source for portable electronics and are intensively pursued for applications in large-scale electric vehicles and sustainable energy storage systems.[1] Since the pioneering work of Goodenough and co-workers, olivine-type cathode materials of $LiFePO_4$ (LFP) and $LiMnPO_4$ (LMP) have been extensively studied owing to their high theoretical capacity (170 and 171 mAh g^{-1}, respectively), thermal stability, and environmental friendliness.[2] LFP is widely present in current commercial batteries. The high power applications of LFP, however, are limited owing to a low energy density of 586 Wh kg^{-1}.[3] Promisingly, LMP offers a 20% higher energy density (701 Wh kg^{-1}) for a higher operating voltage (4.1 V vs. Li/Li^+) than that of LFP (3.45 V vs. Li/Li^+).[4] Although the volume change (6.5%) between LMP (316.41 Å) and delithiated $MnPO_4$ (MP, 296.20 Å) is harmful to the structural stability, the strong covalent bonding between P and O in PO_4 units guarantees a good thermal stability.[5] Nevertheless, LMP is an insulator with extremely low electronic conductivity ($<10^{-9}$ S cm^{-1}) and ionic conductivity (10^{-16}–10^{-14} cm^2 s^{-1}), whereas LFP is a semiconductor.[3c,6] The smooth extraction of Li^+ from the native LMP was found to be very complicated. The main difficulty is kinetic problems resulting from the sluggish diffusion of Li^+ in electrodes. Aside from the sole Li^+ diffusion channel along the preferential [0 1 0] direction, the polaronic holes localized on the Mn^{3+} sites and the strain at the MP/LMP interface were suggested as important rate-limiting factors.[7]

The kinetic problems could be mitigated by particle nanosizing and conductive surface coating,[4,5a,7b,8] as illustrated in Scheme 1a. It is generally believed a homogeneous conducting carbon matrix would facilitate electron transportation, whereas the nanoscale size would provide efficient ionic transport channels and relieve the volume strain. Nevertheless, the electrochemical performance is strongly dependent on the microstructure of the nanoscale LMP. In a review of previous reports, nanosizing does not always result in significantly improved performance of LMP. Doan et al. prepared LMP/C nanocomposites with a size of approximately 100 nm by spray pyrolysis and wet ball-milling followed by heat treatment.[9] The

[a] H. Yang, X. Wang, C. Zhao, Prof. L. Wang, Prof. T. Liu
State Key Laboratory for Modification of Chemical Fibers and Polymer Materials
College of Materials Science and Engineering
Innovation Center for Textile Science and Technology
Donghua University
Shanghai 201620 (PR China)
E-mail: linawang@dhu.edu.cn
txliu@dhu.edu.cn

[b] Dr. J. Liu, Prof. Y. Wang, Prof. Y. Xia
Department of Chemistry
Shanghai Key Laboratory of Molecular Catalysis and Innovative Materials, Institute of New Energy
and Collaborative Innovation Center of Chemistry for Energy Materials
Fudan University
Shanghai 200433 (PR China)

Supporting Information and the ORCID identification number(s) for the author(s) of this article can be found under: https://doi.org/10.1002/cssc.201901377.

© 2019 Wiley-VCH Verlag GmbH & Co. KGaA, Weinheim

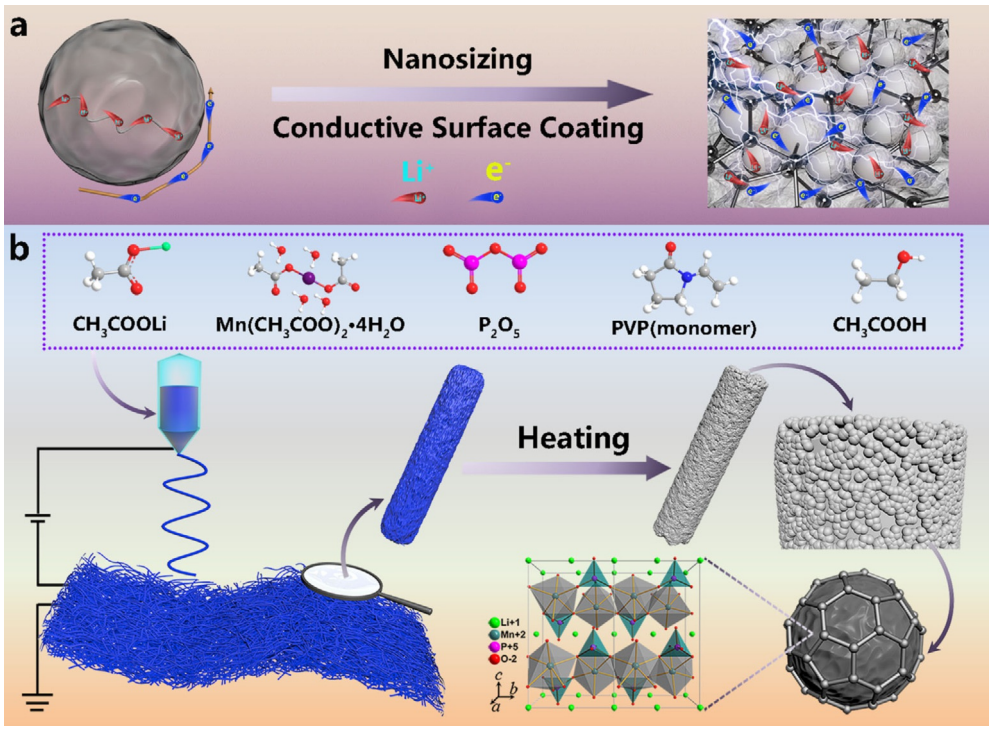

Scheme 1. Structural engineering of LMP. a) Illustration of the improved reaction kinetics of LMP by nanosizing and conductive surface coating. b) Schematic view of the procedure for preparing 1D LMP@C nanofibers with in situ created 3D mesoporous structure.

LMP/C exhibited a discharge capacity of 123 mAh g^{-1} at a galvanostatic charge/discharge rate of 0.05 C (1 C = 171 mA g^{-1}). A rather significantly decreased capacity of 70 mAh g^{-1} was delivered at 0.5 C. Wang et al. assembled carbon layer wrapped LMP nanoplates into microclusters by a microemulsion-based approach, obtaining a practical capacity of 132.6 mAh g^{-1} at 0.1 C and 99.2 mAh g^{-1} at 1 C.[4a]

To date, LMP cathode materials with dramatically enhanced power density combined with high specific capacity and long-term cyclic stability have rarely been acquired. In a micrometer-sized Li-ion battery material, the kinetics of charge storage are generally controlled by the diffusion of Li^+ within the bulk particles. The reaction kinetics in LMP particles at smaller dimensions are not well understood yet. The inspiring work by Dunn and co-workers on metal oxides clearly pointed out that pseudocapacitive behavior can emerge through nanostructuring of a battery material.[10] Quantitative analysis of TiO_2 suggested increased capacitive effects from 15% to 35% by reducing the particle size from 30 to 7 nm.[10b] Pseudocapacitive charge storage through fast surface reactions allows for high charge/discharge rates, offering a means of achieving long cycling life and producing high power density.[10,11] However, a large proportion of capacitive contribution would lead to a weakened delithiation/lithiation voltage platform on the galvanostatic charge/discharge profiles. Okubo et al. revealed the extrinsic pseudocapacitance of the traditional $LiCoO_2$ cathode material.[12] Capacitive behavior became dominant when decreasing the crystallite size to 17 nm or less, reducing the voltage plateau in favor of a continuously sloping voltage profile over the entire intercalation range. On further reducing the crystallite size to 6 nm, the cell exhibited a nearly linear potential–time response, which is an essential electrochemical feature of supercapacitors. In this case, the charge transfer of $LiCoO_2$ is merely limited to the electrode/electrolyte interface without Li^+ diffusion within the bulk material, giving rise to a dramatically decreased capacity ($\approx$70 mAh g^{-1}) of approximately 50% lower than that of the bulk ($\approx$140 mAh g^{-1}). Therefore, great efforts are required in exploring battery-type materials with higher rate performance and capacitance materials with higher capacity. In other words, rational structural engineering and compounding with the conductive material of LMP holds promise to achieve a battery-level energy density as well as a capacitive-like cycling ability and rate capability.

Here, we aim to develop functional LMP that can store and deliver a large amount of Li^+ quickly. One-dimensional (1D) $LiMnPO_4$@carbon (LMP@C) nanofibers with in situ created 3D mesoporous structure are prepared by a facile and versatile electrospinning method. The hierarchical construction prevents the pulverization/aggregation of ultrafine LMP nanoparticles and relieves the lattice strain at the MP/LMP interface upon delithiation/lithiation processes. The electrolyte readily penetrates into the interconnected and exposed mesoporous intersections, providing fast charge transport and promoting pseudocapacitive behavior. The current separation technique allows the quantitative separation of diffusion-controlled and capacitive currents. The increased pseudocapacitive contribution at higher current rates suggests the rapid reaction kinetics of LMP@C nanofibers, leading to a high rate capability and cyclic stability but without compromising the energy density. The LMP@C exhibits a high reversible capacity of 149.8 mAh g^{-1}

© 2019 Wiley-VCH Verlag GmbH & Co. KGaA, Weinheim

with 92% retention over 300 cycles at 0.2 C. Remarkably, more than 60% of the capacity is delivered above 3.9 V. Even at a high rate of 5 C, a specific capacity of 63.1 mAh g^{-1} can still be afforded even after a long lifespan over 2000 cycles with a coulombic efficiency (CE) $\geq$ 98%.

Results and Discussion

Synthesis and characterization

A view of the preparation procedure is illustrated in Scheme 1b. In brief, the precursor fibers were produced by electrospinning an ethanol solution of polyvinylpyrrolidone (PVP), CH_3COOLi, $Mn(CH_3COO)_2{\cdot}4H_2O$, and P_2O_5. Whereby, PVP provides the desirable rheological properties as well as serving as the carbon source. The as-spun fibers were thermally treated in an Ar atmosphere to obtain LMP@C. Scanning electron microscopy (SEM) images show the precursor fibers of LMP@C-8 with a uniform diameter approximately 500 nm (Figure 1a). A wrinkled surface ascribed to the volatilization of ethanol is observed (inset of Figure 1a). After being calcined at 750 °C, the nanofibrous network is well maintained although the average diameter of the nanofibers slightly increasing to approximately 600 nm (Figure 1b). The larger diameter of the annealed fibers is due to the gas release during the heat treatment. In addition, a porous structure is in situ introduced into the nanofibers. The thermogravimetric analysis (TGA) curve of the precursor fiber displays a sharp weight loss of 19.87 wt% at 180–340 °C and 24.39 wt% at 340–490 °C (Figure S1, see the Supporting Information), attributed to the decomposition of metal acetates and carbonization of PVP, respectively. The enlarged surface (Figure 1c) and cross-section views (Figure 1d) show that the nanofibers are composed of interconnected cashew-like nanoparticles. High-resolution transmission electron microscopy (HR-TEM) images show the nanoparticles have an average size of approximately 30×20 nm and are homogeneously distributed in the 3D nanoporous structure of the 1D nanofibers (Figure 1e). The specific surface area of LMP@C-8 is measured to be approximately 45.70 $m^2 g^{-1}$ according to the adsorption isotherm (Figure S2a in the Supporting Information). The type IV curve with a H1-type hysteresis loop is related to the cylindrical channels,[13] indicating a highly mesoporous feature. The average size of the mesopores is 11 nm based on the pore size distribution analysis (Figure S2b in the Supporting Information). The clear lattice fringes with interplanar spacings of 0.305, 0.374, and 0.237 nm correspond to the respective (200), (101), and (002) planes of crystalline LMP, which are embedded in an ultrathin carbon layer of approximately 1 nm (Figure 1f). The selected area electron diffraction (SAED) of the TEM with distinct (113), (200), (140), and (220) planes and broad ring patterns is also in line with the olivine-type LMP (Figure 1g). The homogeneous distribution of Mn, P, O, and C elements throughout the nanofibers was confirmed by energy-dispersive X-ray spectroscopy (EDS) elemental mapping images (Figure 1h). The corresponding elemental analysis suggests the location of Mn, P, and O with the molar ratio close to 1:1:4 (Figure S3 in the Supporting Information), which is consistent with that of LMP.

The morphological features of LMP@C are tunable by controlling the PVP content in the precursor solution and the synthesis temperature. Because of insufficient gas being generated during heating, agglomerated particles can be seen in the porous nanofibers of LMP@C-6 with a lower PVP content in the precursor (Figure S4a in the Supporting Information).

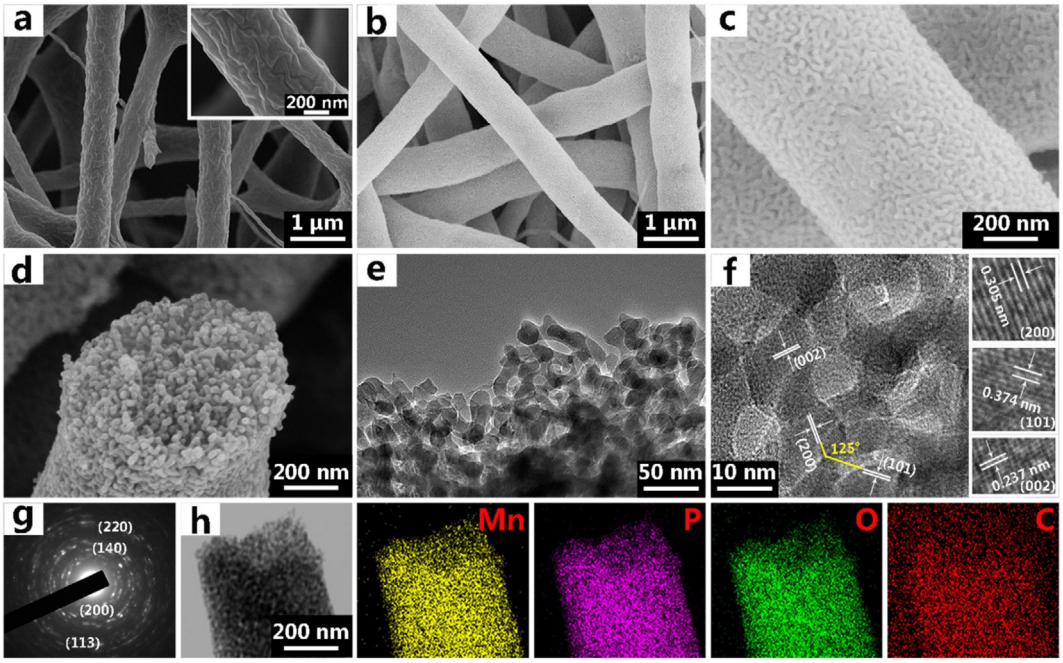

Figure 1. Micrographs of as-electrospun LMP@C-8 nanofibers before and after heat treatment at 750 °C. a) SEM images of precursor fibers with the inset showing the corresponding partially appearance. b–d) SEM images of the surface and cross-sectional views of LMP@C-8 nanofibers. e, f) HR-TEM images. The insets of f) show the lattice fringes. g) SAED pattern. h) TEM-EDS mapping.

© 2019 Wiley-VCH Verlag GmbH & Co. KGaA, Weinheim

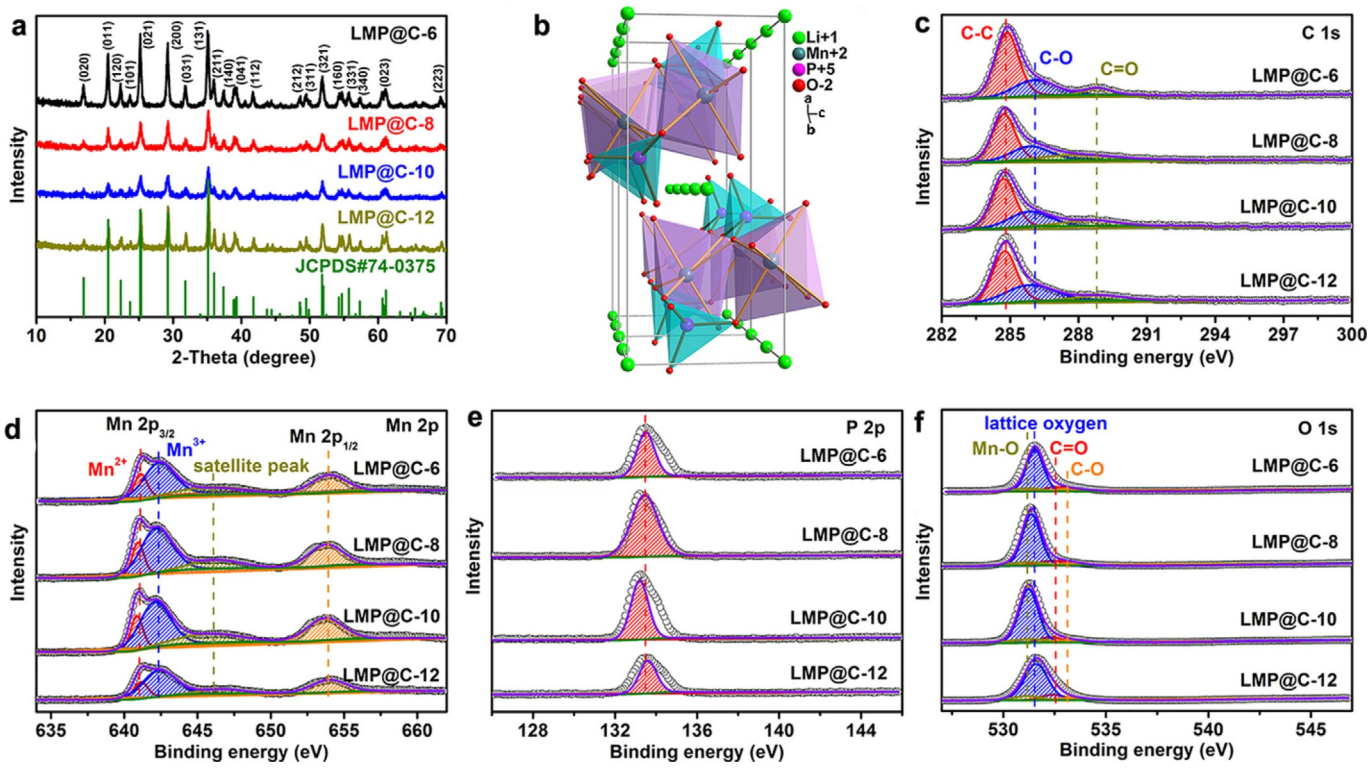

Figure 2. a) XRD pattern of LMP@C nanofibers. b) Crystal structure of LMP depicting the curved trajectory of Li^+ transport along the *b*-axis [0 1 0]. The MnO_6 octahedra are shown in pink, the PO_4 tetrahedral in light blue, and the Li^+ in green. c–f) XPS spectra of LMP@C nanofibers: c) C 1s, d) Mn 2p, e) P 2p, and f) O 1s.

Conversely, the robust gas release resulting from a higher PVP content caused the increase in the fibrous diameter by 100–200 nm for LMP@C-10 (Figure S4b in the Supporting Information) or even collapsed the fibers of LMP@C-12 (Figure S4c in the Supporting Information). The element content analysis summarized in Table S1 (in the Supporting Information) suggests that the carbon contents in LMP@C-6, LMP@C-8, LMP@C-10, and LMP@C-12 are 4.58, 5.77, 6.78, and 7.32 wt%, respectively. The X-ray diffractometer (XRD) patterns in Figure 2a further confirm the crystalline structure of LMP with a *Pnmb* space group (JCPDS#74-0375). The structure consists of a polyoxyanionic framework containing LiO_6 octahedra, MnO_6 octahedra, and PO_4 tetrahedra (Figure 2b). Strong covalence stabilizes the anti-bonding $Mn^{3+/2+}$ state through a Mn-O-P inductive effect, preventing O_2 release in the fully charged state. In addition to the lattice parameters, the calculated grain sizes are summarized in Table 1. The lattice parameters of LMP@C-8 are closer to the standard card parameters. Its calculated grain size is the smallest, that is, 224 Å, in agreement with the TEM observation. Crystalline LMP is also acquired when calcined at 650 and 850 °C (Figure S5 in the Supporting Information). Nevertheless, the lattice parameters and morphology of LMP@C strongly depend on the synthesis temperature. In contrast to 750 °C, a lower or higher temperature would lead to irregular fibers (Figure S6 in the Supporting Information) and a larger grain size (Table S2 in the Supporting Information). The cohesive carbon network at 650 °C (Figure S6a in the Supporting Information) and the high temperature agglomeration at 850 °C (Figure S6b in the Supporting Information) should be responsible for the larger grain size. No peaks belonging to crystalline graphite carbon appear in the diffraction patterns, indicating that the in situ generated carbon from PVP is amorphous and its presence does not influence the structure of LMP. The disorder of carbon identified by the intensity ratio of disorder induced D-band to in-plane vibrational G-band (I_D/I_G) value in the Raman spectra is in the range 0.845–0.856 (Figure S7 in the Supporting Information), reflecting the relatively high degree of ordering in the carbon material.[14]

Table 1. The lattice parameters, grain size, and volume of the unit cell of LMP@C nanofibers.

Sample	*a* [Å]	*b* [Å]	*c* [Å]	*V* [Å^3]	Grain size [Å]
JCPDS#74-0375	6.1000	10.4600	4.7440	302.69	–
LMP@C-6	6.1159	10.4875	4.7618	305.42	384
LMP@C-8	6.1044	10.3905	4.7641	302.18	224
LMP@C-10	6.1276	10.5271	4.7251	304.80	268
LMP@C-12	6.0803	10.4291	4.7340	300.19	288

X-ray photoelectron spectroscopy (XPS) was performed to investigate the surface chemistry of the LMP@C composites for their intrinsic sensitivity when exposed in air. The XPS spectra clearly show peaks of Li, Mn, P, O, and C elements (Figure S8 in the Supporting Information). The C 1s spectra are classified into C—C (284.70 eV), C—O (286.04 eV), and C=O (287.94 eV)[15] (Figure 2c). The Mn 2p spectra are split into two peaks owing

© 2019 Wiley-VCH Verlag GmbH & Co. KGaA, Weinheim

to spin-orbit coupling (Mn $2p_{3/2}$ and Mn $2p_{1/2}$) with a "shake-up" satellite[16] (Figure 2d). The peaks detected at 653 eV correspond to the Mn $2p^{1/2}$ of Mn^{2+}, whereas the Mn $2p_{3/2}$ spectra center at 641.00 and 642.10 eV, corresponding to the Mn^{2+} and Mn^{3+} oxidation states.[17] However, no significant impurities are detected from the XRD results in Figure 2a, indicating the trace amount of Mn^{3+}. The coexistence of Mn^{3+} should be due to the instability of Mn^{2+} during synthesis at high temperature or when the LMP@C is exposed to the ambient atmosphere. The satellite peak at 647 eV is the characteristic peak of bivalent Mn.[16,18] The P 2p spectral peak at 133.20 eV is attributed to the PO_4^{3-} group[19] (Figure 2e). In Figure 2f, the fitted O 1s peaks at 533.4 and 532.5 eV are attributed to the C–O and C=O bands, respectively.[20] The peak near 531.1 eV is related to the Mn–O band, which is attributed to the bond between the fringe O and Mn of LMP.[21] The structural characteristics of LMP@C-8 include 3D mesoporous iso-oriented interconnected ultrafine LMP nanocrystals, ultrathin carbon coating layer, high active material loading, and high surface area, which are vital for superior Li^+ storage performance.

Li^+ storage performance and reaction kinetics

To get an insight into the Li^+ storage behavior of LMP@C nanofibers, galvanostatic cycles were first performed under the same charge and discharge rates between 2.0 and 4.5 V (vs. Li/Li^+) without using a constant voltage mode at 4.5 V. At 0.2 C (1 C = 171 mA g^{-1}), the LMP@C-8 delivers an initial specific discharge capacity of 162.4 mAh g^{-1} with 92% capacity retention after 300 cycles and a CE of 95% (Figure 3a). The capacity and cyclic performance are the best among the LMP@C electrodes (Figure S9a in the Supporting Information). Compared with that of LMP@C-6, LMP@C-10, and LMP@C-12, the electrochemical impedance spectroscopy (EIS) profile of LMP@C-8 shows the smallest charge transfer resistance (R_{ct}) of 155 Ω (Figure S9b in the Supporting Information). The redox plateau potentials arising from Mn^{2+}/Mn^{3+} are clearly observed at 4.2 and 4.0 V in the charge and discharge voltage profiles, respectively (Figure 3b). Accordingly, one pair of current peaks that can be ascribed to the Mn^{2+}/Mn^{3+} redox couple is present in the cyclic voltammetry (CV) curves for ten cycles at a sweep

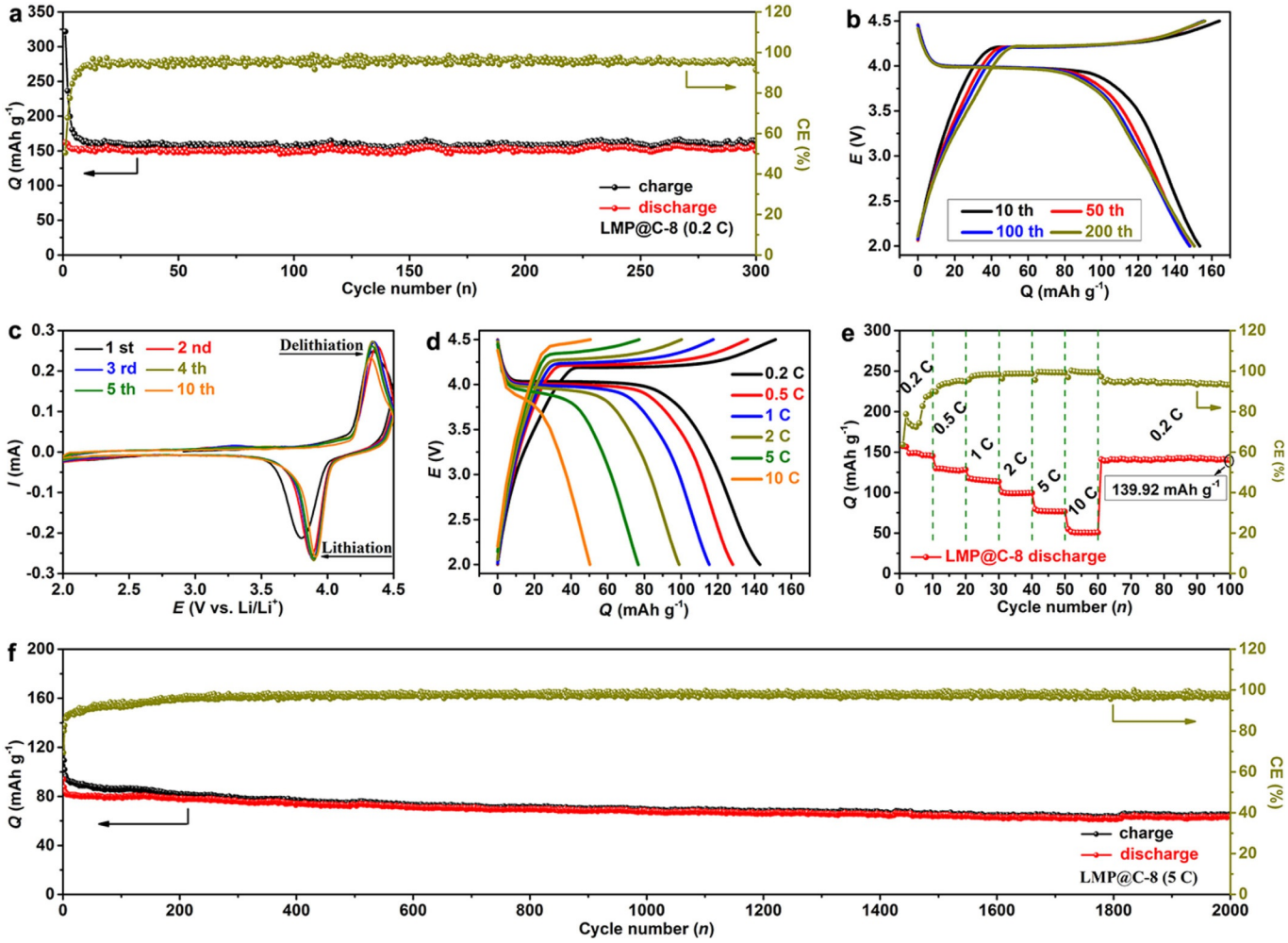

Figure 3. Electrochemical performance of LMP@C-8 electrodes. a) Cycling profiles with respect to specific capacity (*Q*) and coulombic efficiency (CE) over 300 cycles at 0.2 C (1 C = 171 mA g^{-1}). b) The corresponding representative voltage–capacity profiles. c) CV curves at a sweep rate of 0.2 mV s^{-1} for ten cycles. d) Voltage–capacity profiles at various current rates from 0.2 to 10 C. e) The corresponding rate capability. f) Cycling profiles with respect to *Q* and CE up to 2000 cycles at 5 C.

© 2019 Wiley-VCH Verlag GmbH & Co. KGaA, Weinheim

rate of 0.2 mV s^{-1} (Figure 3c). After the first cycle, the subsequent CV curves are highly overlapped without any noticeable peak shift, indicating the excellent stability and high reversibility. The SEM image shows that the 1D fibrous morphology with 3D porous structure of LMP@C-8 is well maintained after 300 cycles (Figure S10 in the Supporting Information). On increasing the current density to 0.5, 1, 2, 5, and 10 C, the reversible capacity reaches 128.1, 115.3, 98.9, 76.7, and 50.3 mAh g^{-1} on the fifth cycle of each current density, respectively (Figure 3d). On going from 10 to 0.2 C, a high capacity of 141 mAh g^{-1} can be recovered rapidly, exhibiting a strong tolerance for the rapid Li^+ extraction/insertion (Figure 3e). To estimate the long lifespan Li^+ storage under fast charge and discharge, the electrode was galvanostatically operated at 5 C (Figure 3f). Impressively, a specific capacity of 63 mAh g^{-1} can be afforded even after 2000 cycles with a CE $\geq$ 98%.

When operated at a narrow cut-off voltage window of 2.7–4.5 V, the LMP@C-8 is able to deliver a reversible capacity of 139, 103.3, 82.2, 65.8, and 44.6 mAh g^{-1} (Figure S11a in the Supporting Information) with a stable cycling (Figure S11b in the Supporting Information) at 0.2, 0.5, 1, 2, and 5 C, respectively. On reducing the carbon additive to 10 wt% in the electrodes, the LMP@C-8 delivers a relatively decreased capacity of 133.2, 102.2, 78.2, 57.4, and 27.8 mAh g^{-1} (Figure S12a in the Supporting Information) at 0.2, 0.5, 1, 2, and 5 C, respectively. Nevertheless, the stable cycling is still maintained (Figure S12b in the Supporting Information). From the results presented herein, the charge and discharge rates are the same for both high output power and fast charging applications. To the best of our knowledge, the electrochemical performance of LMP@C-8 nanofibers is among the best results achieved with LMP materials (Table S3 in the Supporting Information). Hagen et al. prepared a type of LMP-based nanofibers without a porous structure, giving rise to a relatively low discharge specific capacity of approximately 50 mAh g^{-1} at 0.5 C in a constant-current–constant-voltage (CC-CV) mode upon charging.[22] With the same CC-CV mode, the LMP@C-8 could deliver a higher reversible capacity of 127 mAh g^{-1} at 0.5 C and 92 mAh g^{-1} at 5 C (Figure S13a in the Supporting Information). With 10 wt% carbon additive in the electrodes, approximately 100 mAh g^{-1} at 0.5 C can be obtained (Figure S13b in the Supporting Information). The unique nanofibrous architecture, especially the interconnected mesoporous channels, means that each individual LMP crystallite is readily accessible to the liquid electrolyte. As a consequence, a high specific capacity, rate capability, and cyclic stability are achieved, ascribed to the short transport path for both the electrons through the interconnected carbon walls and the Li^+ within single LMP nanocrystalline grains. In addition to the improved ion transport kinetics, the size effects are expected also to help alleviate the strain at the MP/LMP interface.

To understand the improved electrochemical performance, CV measurements at various sweep rates from 0.05 to 0.5 mV s^{-1} were conducted (Figure 4a). The potential difference between the cathodic and anodic peak slightly increases with increasing sweep rates. The Randles–Sevcik equation [Eq. (1)] has been used to evaluate the diffusion kinetics of Li^+ insertion materials during a charge/discharge process:[23]

$$I_P = 2.69 \times 10^5 A C_{Li} D_{Li}^{1/2} n^{3/2} \nu^{1/2} \quad (1)$$

where I_P is the peak current (A), A is the electrode area (cm^2), and C_{Li} is the molar concentration of Li^+ in LMP. The unit cell volume of LMP is calculated to be a (6.1000 Å) × b (10.4600 Å) × c (4.7440 Å) = 302.70×10^{-24} cm^3, thereby, 1 cm^3 contains $1/(302.70\times10^{-24}) = 3.30\times10^{21}$ unit cells. As every LMP cell contains four Li^+, 1 cm^3 contains $4\times3.30\times10^{21}/(6.02\times10^{23}) = 2.20\times10^{-2}$ mol Li^+. This means the Li^+ concentration is approximately 2.20×10^{-2} mol cm^{-3}.[24] D_{Li} is the Li^+ diffusion coefficient at 298 K, n is the number of electrons involved in the redox process ($n=1$ for Mn^{2+}/Mn^{3+} redox pair), and ν is the sweep rate (V s^{-1}). According to the slope of the peak currents (I_P) versus the square root of scan rates ($\nu^{1/2}$) plotted in Figure 4b, the Li^+ diffusion coefficients of LMP@C-8 are calculated to be 2.06×10^{-12} and 2.41×10^{-12} cm^2 s^{-1} for the charge and discharge processes, respectively. The high Li^+ diffusion coefficients are attributed to the continuous and rapid ion diffusion pathways afforded by the mesoporous nanofibers with large surface area.

Notably, the sloping voltages rather than plateaus at distinct voltages are present in the latter part of the galvanostatic profiles. Take the tenth cycle at 0.2 C, for instance, the high plateau capacity above 3.9 V is 97 mAh g^{-1}, accounting for 63% of the total capacity (Figure 4c). The sloping voltage profile is an indication of pseudocapacitive behavior. Assuming that the measured peak current (I_P) obeys a power-law relationship with the sweep rate (ν) of CV, the relationship is expressed as Equation (2):[10a,25]

$$I_P = a\nu^b \quad (2)$$

where a and b are adjustable values. A higher b value suggests faster reaction kinetics. Whereas a b value of 0.5 would indicate that the current is controlled by a semi-infinite linear diffusion, and a value of 1 indicates that the current is surface-controlled. In terms of the $\log I_P$ versus $\log \nu$ plots shown in Figure 4d, the b values of the cathodic and anodic peaks are approximate, which are 0.57 and 0.59, respectively. A b value above 0.5 indicates the current is not simply from a diffusion-controlled intercalation reaction. As a control, a carbon-free bulk LMP with a nanosheet morphology (Figure S14a in the Supporting Information) was synthesized. The XRD pattern in Figure S14b (in the Supporting Information) confirms the crystalline structure of LMP with a *Pnmb* space group (JCPDS#74-0375). From the CV of the bulk LMP at various sweep rates (Figure S14c in the Supporting Information), we calculated the b values of cathode and anode peaks were 0.41 and 0.48, respectively (Figure S14d in the Supporting Information). A low b value of less than 0.5 suggests the current is controlled by diffusion, that is, slow reaction kinetics. Instead, the b values of the cathodic current plotted as a function of potential in the overall voltage range are between 0.5 and 1.0, shedding more light on the reaction kinetics of LMP@C-8 nanofibers (Figure 4e). The charge storage mechanisms are therefore consid-

© 2019 Wiley-VCH Verlag GmbH & Co. KGaA, Weinheim

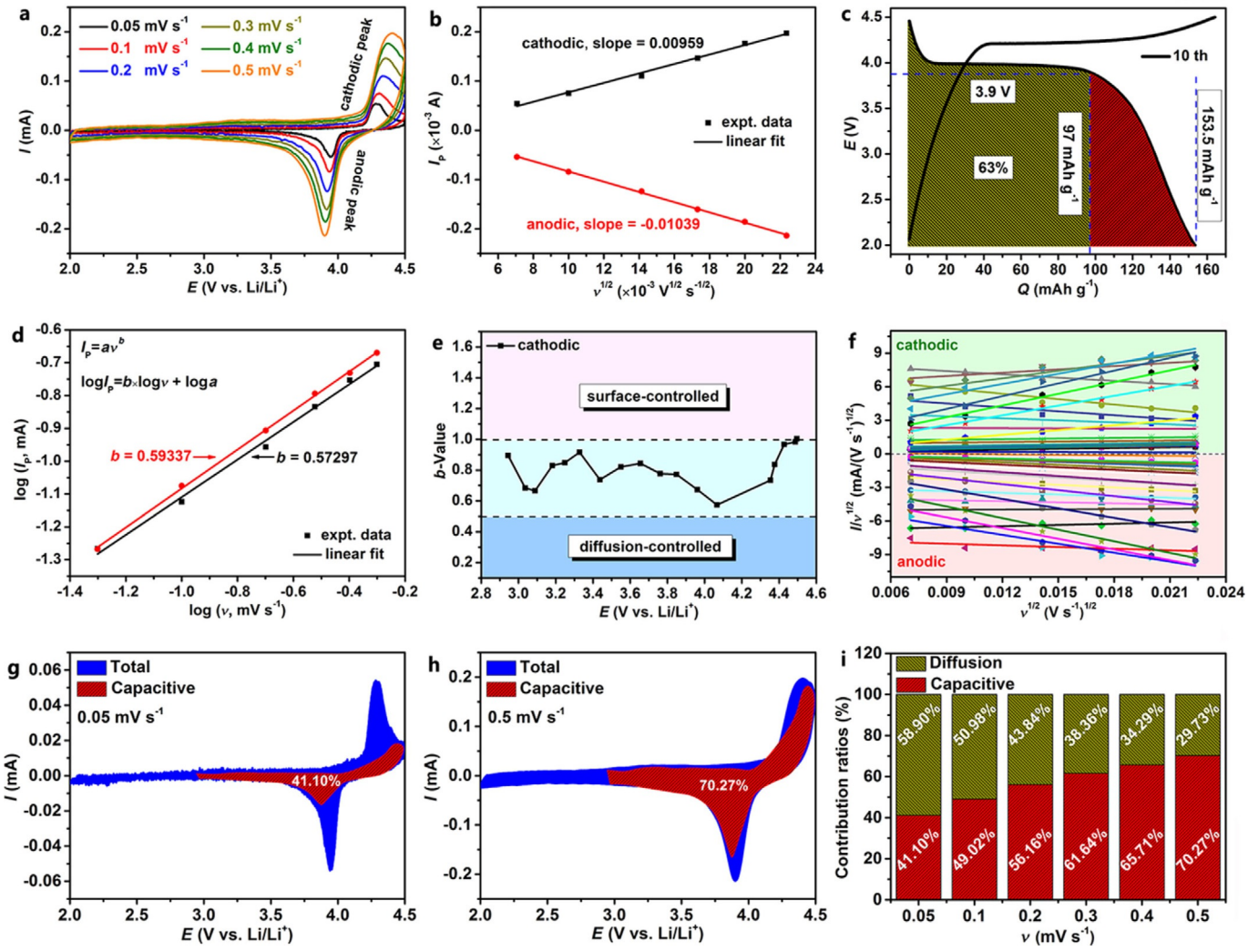

Figure 4. Analysis of the electrochemical reaction kinetics of LMP@C-8 electrodes. a) CV curves at various sweep rates of 0.05, 0.1, 0.2, 0.3, 0.4, and 0.5 mV s^{-1}. b) Relationship of the peak currents (I_p) versus the square root of scan rates ($v^{1/2}$). c) The ratio of the high plateau capacity above 3.9 V at the tenth cycle at 0.2 C. d) Relationship between the logarithm of peak currents (log I_p) and the logarithm of sweep rates (log v). e) Calculated *b* values as a function of potential for the cathodic current. f) Plots of $I/v^{1/2}$ vs. $v^{1/2}$ at 36 different potentials within 2.0–4.5 V. g, h) CV curves at 0.05 and 0.5 mV s^{-1} with the red area representing the capacitive contribution. i) Normalized contribution ratio of capacitive (red) and diffusion-controlled (dark yellow) capacities at various sweep rates.

ered as faradaic contributions from synergic diffusion-controlled intercalation reactions and surface capacitive charge transfer. The percentage of the capacitive contribution at different scan rates is quantified through the Trasatti analysis according to Dunn et al.:[10b]

$$I = k_1 \times \nu + k_2 \times \nu^{1/2} \quad (3)$$

where the whole current (I) is separated into the current from the surface-controlled pseudocapacitive effect ($k_1 \times \nu$) and the diffusion-controlled process ($k_2 \times \nu^{1/2}$). The above equation can also be reformulated as Equation (4):

$$I/\nu^{1/2} = k_1 \times \nu^{1/2} + k_2 \quad (4)$$

By plotting $I/\nu^{1/2}$ versus $\nu^{1/2}$ at 18 different fixed potentials in the range 2.0–4.5 V for both cathodic and anodic sweeps, 36 separate curves are obtained (Figure 4 f). The linear behavior enables us to determine k_1 and k_2 from the slope and the *y*-axis intercept point of the straight line, respectively, at each fixed potential. From this procedure, the currents arising from diffusion-controlled and capacitive processes are able to be distinguished quantitatively.

A capacitive contribution of 41.10% is identified at 0.05 mV s^{-1} (Figure 4 g). Generally, the capacitive contribution increases gradually with increasing sweep rates (Figure S15 in the Supporting Information). The surface-dominated pseudocapacitance is regarded as a major Li^+ storage mechanism at a high sweep rate, which tends to be 70.27% at 0.5 mV s^{-1} (Figure 4 h). The depressed diffusion and dominant capacitive contribution at higher scan rates are more clearly illustrated in Figure 4 i. The CV curves at various scan rates in the voltage window 2.7–4.5 V are shown in Figure S16 a (in the Supporting Information). Compared with the cell operated within 2.0–4.5 V, a higher capacitive contribution is present at various scan rates (Figure S16 b in the Supporting Information). For ex-

© 2019 Wiley-VCH Verlag GmbH & Co. KGaA, Weinheim

ample, capacitive contributions of 49.44% and 72.28% are identified at 0.05 and 0.5 mV s^{-1} (Figure S16c and S16d in the Supporting Information), respectively. To clarify the effect of carbon additive, we further calculated the capacitive contribution from CV curves with 10 wt% carbon additive in the electrode within 2.0–4.5 V (Figure S17a in the Supporting Information). Generally, the capacitive contribution is decreased compared with that with 20 wt% carbon additive at various sweep rates (Figure S17b in the Supporting Information). A capacitive contribution of 21.47% is identified at 0.05 mV s^{-1} (Figure S17c in the Supporting Information), but a high value of 49.09% is still present at 0.5 mV s^{-1} (Figure S17d in the Supporting Information). The result is unsurprising considering the mesoporous electrode architecture with a crystalline size of LMP@C less than 40 nm. A high internal surface area enables the electrolyte to kinetically access the majority of Li^+ located on the surface sites of nanofibers quickly.

Structure evolution at varying charge/discharge states

To investigate phase evolution and surface states of the LMP@C-8 electrode, XRD and XPS were conducted at varying depths of charge/discharge. Figure 5a shows the galvanostatic voltage profiles for the first two cycles at 0.2 C with labeled points for XRD and XPS, where 1C-4.5 V, for example, represents charging to 4.5 V on the first cycle and 2D-3.9 V means discharging to 3.9 V on the second cycle and so on. The crystal structures of the LMP@C-8 electrodes at various voltage states were first investigated by XRD (Figure 5b). The main characteristic diffraction peaks are almost coincident except for a regular change at the 16.94 and 31.82° positions. Being distinguished from that of the pristine electrode, the diffraction peaks at these two-degree positions become weak at the intermediate charge of 4.2 V and almost invisible at the full charge of 4.5 V. This process corresponds to the two-phase transformation from LMP to L_xMP ($0 < x \leq 1$) with the extraction of Li^+. The peaks appear again upon discharging to 3.9 V and further to 2.0 V irrespective of whether it is the first or second cycle. The results demonstrate that the electrochemical behavior of the LMP@C-8 electrode is a reversible process of Li^+ extraction/insertion ($LMP \rightleftarrows MP + Li^+ + e^-$). The XPS spectra of Mn 2p validate the Mn^{3+} valence of the fully charged product and the recovery of Mn^{2+} after being fully discharged (Figure 5c). The disappearance of the characteristic Li 1s peak at 4.5 V and recovery at 2.0 V further verify the two-phase translation between LMP and MP (Figure 5d). The olivine structure is stable during the repeated charge/discharge processes, as a result of the phase transfer illustrated in Figure 5e.

Conclusions

We synthesized 1D $LiMnPO_4$ (LMP)@C nanofibers with a 3D mesoporous architecture through a feasible electrospinning method followed by a simple heat treatment. The morphology is strongly depended on the synthesis conditions. By adjusting the concentration of polyvinylpyrrolidone (PVP) and temperature, mesopores are in situ introduced among the interconnected LMP@C nanoparticles. In addition, an ultrathin carbon layer is generated on the ultrafine LMP nanoparticles. The hierarchical structure allows more active sites to be exposed into the electrolyte and relieves the lattice strain during phase translation between LMP and $MnPO_4$. The positive contribution of a surface pseudocapacitive behavior induces fast charge transport but without compromising the high-voltage platform

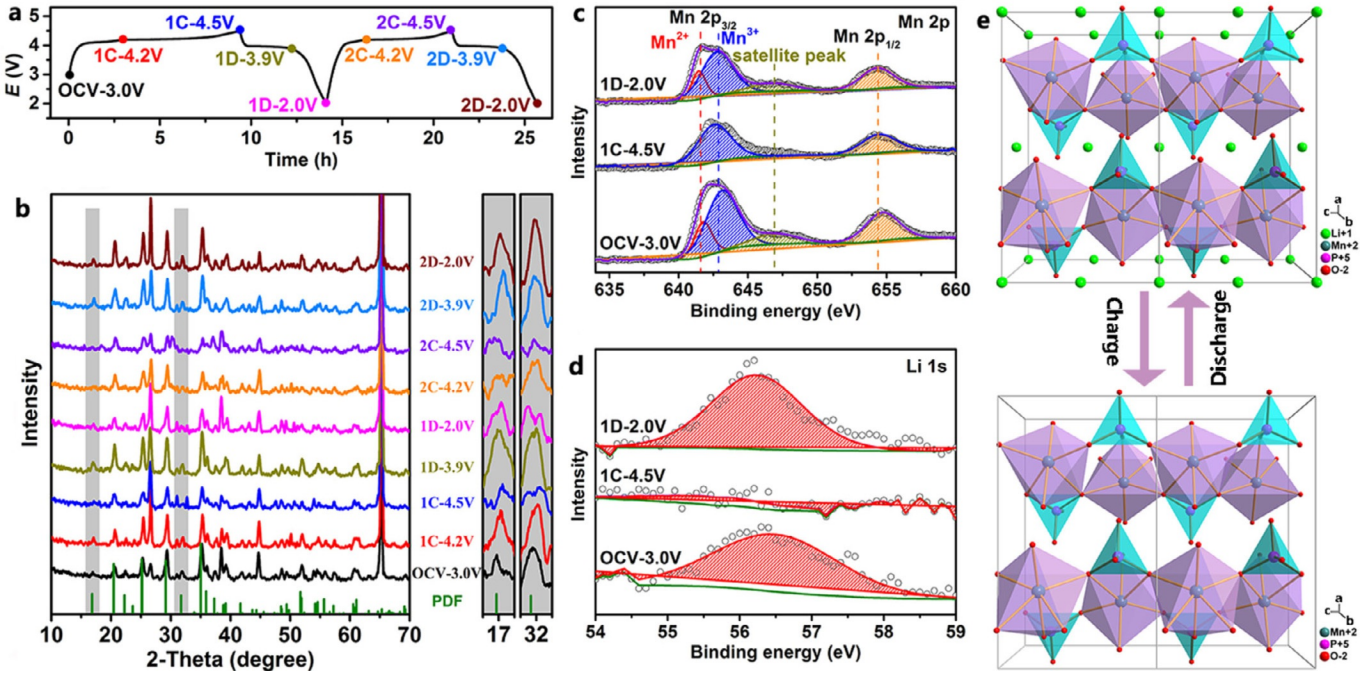

Figure 5. Phase evolution and surface states of LMP@C-8 electrodes during charge/discharge processes. a) The first and second charge/discharge profiles at 0.2 C with labeled points for ex situ XRD and XPS. b) Ex situ XRD evolution at different charge/discharge potentials. c, d) XPS spectra of Mn 2p and Li 1s at the open-circuit voltage (OCV), 1C-4.5 V and 1D-2.0 V, respectively. e) Crystal structure of LMP during reversible Li^+ extraction/insertion.

© 2019 Wiley-VCH Verlag GmbH & Co. KGaA, Weinheim

capacity much. An initial discharge capacity of 162.4 mAh g^{-1} is delivered with 149.8 mAh g^{-1} retained upon 300 cycles at 0.2 C. Even at a high rate of 5 C, an impressive specific capacity of 63.1 mAh g^{-1} still can be afforded after 2000 cycles along with a CE above 98%, proving the long lifespan Li^+ storage ability under fast charge and discharge.

Experimental Section

Synthesis of LMP@C nanofibers

PVP (M_w = 1300000) was purchased from Aldrich Reagent Company. CH_3COOLi (99%, Sigma–Aldrich), $Mn(CH_3COO)_2{\cdot}4H_2O$ (98%, Sigma–Aldrich), P_2O_5 (99.8%, Sinopharm), and CH_3CH_2OH (99.8%, Sinopharm) were used as received. LMP@C nanofibers were synthesized by using a one-step electrospinning technique followed by a heat treatment. Typically, CH_3COOLi (6 mmol), $Mn(CH_3COO)_2{\cdot}4H_2O$ (6 mmol), and P_2O_5 (3 mmol, 2:2:1, molar ratio) were dissolved in ethanol (12 mL) under vigorous stirring at 50 °C for 2 h. PVP (0.8 g, the mass ratio of PVP to ethanol is 8%) was then added and stirred overnight at 30 °C. The homogeneous precursor solution was loaded into a plastic syringe equipped with a 10-gauge blunt-tip needle. The needle was electrically connected to a high-voltage power supply. A voltage of 15 kV was applied between it and an aluminium foil to initiate the electrospinning. The flowing rate was controlled to be 0.8 μL min^{-1} by using a syringe pump. The aluminium foil was ground and placed 20 cm away from the needle tip to collect the precursor fibers.

The dried precursor fibers were calcined at 750 °C for 6 h in an argon (Ar) atmosphere at a rate of 5 °C min^{-1}. The as-prepared product is marked as LMP@C-8. In addition, other LMP@C samples were prepared by using the same route, except varying the amount of PVP (0.6, 1, or 1.2 g) added in the precursor solution. The corresponding products were designated as LMP@C-6, LMP@C-10, and LMP@C-12. As a control, different heating temperatures of 650 and 850 °C were applied to the precursor fibers with 0.8 g PVP to obtain the products LMP@C-8-650 and LMP@C-8-850, respectively.

Synthesis of bulk LMP

LiH_2PO_4 (99%, Aladdin), $Mn(CH_3COO)_2{\cdot}4H_2O$ (98%, Sigma–Aldrich), and $C_4H_{10}O_3$ (99.0%, Sinopharm) were used as received. Typically, $Mn(CH_3COO)_2{\cdot}4H_2O$ (60 mmol), deionized water (30 mL), and $C_4H_{10}O_3$ (200 mL) were added into a three-necked round-bottom flask and stirred in an oil bath at 100 °C for 1 h. Then, 2 M LiH_2PO_4 aqueous solution (30 mL) was added dropwise at a rate of 1 mL min^{-1}. The obtained solution was continually stirred at 100 °C for 4 h. After cooling to room temperature, it was centrifuged, washed thoroughly with ethanol, and finally dried under vacuum at 120 °C overnight to obtain the bulk LMP.

Material characterizations

The morphology of LMP@C was observed by field-emission SEM (S-4800, HITACHI). HR-TEM and SAED measurements were also carried out with a transmission electron microscope (JEOL JEM-2100F). The crystal structures and phase analysis were detected by using an XRD (D/max-2500VB + /PC, Rigaku) equipped with CuK_α radiation at a scan rate of 4° min^{-1}. Raman spectra were recorded by using a Raman Spectrometer (inVia-Reflex, Renishaw). The nitrogen sorption/desorption measurements were performed with a Quadrasorb adsorption instrument (Quantachrome Instruments). The specific surface area was calculated by using the multi-point Brunauer–Emmett–Teller (BET) method. The pore size distributions were calculated from nitrogen sorption data by using the nonlocal density functional theory (NLDFT) equilibrium model method for slit pores. XPS analyses were performed with a spectrometer (Escalab 250Xi) with AlK_α X-ray radiation. Thermogravimetry (TG) was conducted with a TG-DSC analyzer (NETZSCH TG 209 F1 Libra).

Electrochemical measurements

Unless specified otherwise, when preparing the electrodes, a black viscous slurry consisting of LMP@C or bulk LMP, Ketjenblack carbon (KB carbon, ECP-600JD), and poly(vinylidene fluoride) (PVdF) with a mass ratio of 70:20:10 dispersed in *N*-methyl-2-pyrrolidone (NMP) was cast onto an aluminium foil. The electrodes were dried under vacuum at 120 °C overnight to remove NMP before being punched into disks with a diameter (*d*) of 12.0 mm. The average loading of LMP was approximately 3 mg cm^{-2}. Electrochemical tests were carried out under ambient temperature by using CR2025-type coin cells. High-purity metallic lithium electrodes (d = 14 mm, 0.3 mm thick) were separated from the working electrodes by using a Celgard separator (d = 16 mm, 25 μm thick). The electrolyte was 1.0 M $LiPF_6$ dissolved in ethylene/dimethyl carbonate/diethyl carbonate (EC/DMC/DEC, 1:1:1, *v*/*v*/*v*). The cells were assembled in an Ar-filled glovebox (Mikrouna Universal). Galvanostatic charge/discharge tests were carried out with a LAND Battery testing system (CT2001A) within 2.0–4.5 V (vs. Li/Li^+). The applied current densities and the specific capacity values were calculated based on the mass of LMP. CV at various scan rates from 0.05 to 0.5 mV s^{-1} was measured by using an electrochemical workstation (Arbin Instruments, USA). EIS with an AC perturbation signal of 5.0 mV in the frequency range 100 kHz–100 mHz were recorded with a CHI660C electrochemical workstation (Shanghai Chenhua, China).

Acknowledgements

The authors acknowledge funding support from the National Natural Science Foundation of China (21603030 and 51433001), the Natural Science Foundation of Shanghai (17ZR1446400), the Fundamental Research Funds for the Central Universities (2232018D3-02), the Program of Shanghai Academic Research Leader (17XD1400100), and the Shanghai Scientific and Technological Innovation Project (18JC1410600).

Conflict of interest

The authors declare no conflict of interest.

Keywords: batteries · charge storage · lithium manganese phosphate · nanofibers · pseudocapacitance

[1] a) B. Dunn, H. Kamath, J.-M. Tarascon, *Science* **2011**, *334*, 928; b) K. Ariyoshi, T. Ohzuku, *J. Power Sources* **2007**, *174*, 1258; c) Y.-T. Zhou, J. Yang, H.-Q. Liang, J.-K. Pi, C. Zhang, Z.-K. Xu, *Composites Commun.* **2018**, *8*, 46.

[2] a) A. K. Padhi, K. S. Nanjundaswamy, J. B. Goodenough, *J. Electrochem. Soc.* **1997**, *144*, 1188; b) B. Kang, G. Ceder, *Nature* **2009**, *458*, 190; c) M. K. Devaraju, I. Honma, *Adv. Energy Mater.* **2012**, *2*, 284.

© 2019 Wiley-VCH Verlag GmbH & Co. KGaA, Weinheim

[3] a) J.-M. Tarascon, M. Armand, *Nature* **2001**, *414*, 359; b) J. Yang, J. Wang, Y. Tang, D. Wang, X. Li, Y. Hu, R. Li, G. Liang, T.-K. Sham, X. Sun, *Energy Environ. Sci.* **2013**, *6*, 1521; c) Y. Zou, S. Chen, X. Yang, N. Ma, Y. Xia, D. Yang, S. Guo, *Adv. Energy Mater.* **2016**, *6*, 1601549.

[4] a) C. Wang, S. Li, Y. Han, Z. Lu, *ACS Appl. Mater. Interfaces* **2017**, *9*, 27618; b) H. Yoo, M. Jo, B.-S. Jin, H. S. Kim, J. Cho, *Adv. Energy Mater.* **2011**, *1*, 347; c) V. Aravindan, J. Gnanaraj, Y. S. Lee, S. Madhavi, *J. Mater. Chem. A* **2013**, *1*, 3518.

[5] a) Y. Dong, L. Wang, S. Zhang, Y. Zhao, J. Zhou, H. Xie, J. B. Goodenough, *J. Power Sources* **2012**, *215*, 116; b) Y. H. Jung, W. B. Park, M. Pyo, K.-S. Sohn, D. Ahn, *J. Mater. Chem. A* **2017**, *5*, 8939.

[6] a) S. Li, X. Meng, Q. Yi, J. A. Alonso, M. T. Fernández-Díaz, C. Sun, Z. L. Wang, *Nano Energy* **2018**, *52*, 510; b) Y. Deng, C. Yang, K. Zou, X. Qin, Z. Zhao, G. Chen, *Adv. Energy Mater.* **2017**, *7*, 1601958.

[7] a) L. Wang, F. Zhou, G. Ceder, *Electrochem. Solid-State Lett.* **2008**, *11*, A94; b) L. Bao, G. Xu, J. Wang, H. Zong, L. Li, R. Zhao, S. Zhou, G. Shen, G. Han, *CrystEngComm* **2015**, *17*, 6399.

[8] a) J. Zheng, C. Qin, T. Wu, S. Xie, L. Ni, M. Peng, Y. Tang, Y. Chen, *J. Mater. Chem. A* **2015**, *3*, 15299; b) K. Wang, Y. Wang, C. Wang, Y. Xia, *Electrochim. Acta* **2014**, *146*, 8; c) S.-M. Oh, S.-W. Oh, C.-S. Yoon, B. Scrosati, K. Amine, Y.-K. Sun, *Adv. Funct. Mater.* **2010**, *20*, 3260; d) Y. Wang, C.-Y. Wu, H. Yang, J.-G. Duh, *J. Mater. Chem. A* **2018**, *6*, 10395; e) H. Yang, Y. Wang, J.-G. Duh, *ACS Sustainable Chem. Eng.* **2018**, *6*, 13302; f) J. Li, S. Luo, Q. Wang, S. Yan, J. Feng, H. Liu, X. Ding, P. He, *Electrochim. Acta* **2018**, *289*, 415.

[9] T. N. L. Doan, I. Taniguchi, *J. Power Sources* **2011**, *196*, 1399.

[10] a) P. Simon, Y. Gogotsi, B. Dunn, *Science* **2014**, *343*, 1210; b) J. Wang, J. Polleux, J. Lim, B. Dunn, *J. Phys. Chem. C* **2007**, *111*, 14925; c) V. Augustyn, P. Simon, B. Dunn, *Energy Environ. Sci.* **2014**, *7*, 1597.

[11] D. Tie, S. Huang, J. Wang, J. Ma, J. Zhang, Y. Zhao, *Energy Storage Mater.* **2019**, https://doi.org/10.1016/j.ensm.2018.12.018.

[12] M. Okubo, E. Hosono, J. Kim, M. Enomoto, N. Kojima, T. Kudo, H. Zhou, I. Honma, *J. Am. Chem. Soc.* **2007**, *129*, 7444.

[13] S. Sun, C. M. Ghimbeu, R. Janot, J.-M. Le Meins, A. Cassel, C. Davoisne, C. Masquelier, C. Vix-Guterl, *Microporous Mesoporous Mater.* **2014**, *198*, 175.

[14] C. Portet, G. Yushin, Y. Gogotsi, *Carbon* **2007**, *45*, 2511.

[15] B. L.-H. Hu, F.-Y. Wu, C.-T. Lin, A. N. Khlobystov, L.-J. Li, *Nat. Commun.* **2013**, *4*, 1687.

[16] J.-W. Lee, M.-S. Park, B. Anass, J.-H. Park, M.-S. Paik, S.-G. Doo, *Electrochim. Acta* **2010**, *55*, 4162.

[17] a) Z. P. Lu, X. J. Lu, J. J. Ding, T. Zhou, T. Ge, G. Yang, F. Yin, M. F. Wu, *Appl. Surf. Sci.* **2017**, *426*, 19; b) Z. H. Xiao, Y. He, X. L. Li, L. Y. Zhang, Z. Q. Ding, *ChemistrySelect* **2018**, *3*, 4222; c) J. G. Zheng, L. Ni, Y. W. Lu, C. C. Qin, P. X. Liu, T. F. Wu, Y. F. Tang, Y. F. Chen, *J. Power Sources* **2015**, *282*, 444; d) L. Chen, B. Yan, Y. F. Xie, S. M. Wang, X. F. Jiang, G. Yang, *J. Power Sources* **2014**, *261*, 188.

[18] Y. Gao, L. Zhang, S. Feng, W. Shen, S. Guo, *J. Solid State Electrochem.* **2018**, *22*, 285.

[19] C. Gao, J. Zhou, G. Liu, L. Wang, *Appl. Surf. Sci.* **2018**, *433*, 35.

[20] C. X. Zhao, Y. Zhang, S. Z. Deng, N. S. Xu, J. Chen, *J. Alloys Compd.* **2016**, *672*, 433.

[21] B. J. Tan, K. J. Klabunde, P. M. A. Sherwood, *J. Am. Chem. Soc.* **1991**, *113*, 855.

[22] R. von Hagen, H. Lorrmann, K.-C. Möller, S. Mathur, *Adv. Energy Mater.* **2012**, *2*, 553.

[23] Y. Zhao, L. Peng, B. Liu, G. Yu, *Nano Lett.* **2014**, *14*, 2849.

[24] J.-Z. Guo, P.-F. Wang, X.-L. Wu, X.-H. Zhang, Q. Yan, H. Chen, J.-P. Zhang, Y.-G. Guo, *Adv. Mater.* **2017**, *29*, 1701968.

[25] a) H. Lindström, S. Södergren, A. Solbrand, H. Rensmo, J. Hjelm, A. Hagfeldt, S.-E. Lindquist, *J. Phys. Chem. B* **1997**, *101*, 7717; b) X. Dong, L. Chen, J. Liu, S. Haller, Y. Wang, Y. Xia, *Sci. Adv.* **2016**, *2*, e1501038; c) Y. Tao, Y. Wei, Y. Liu, J. Wang, W. Qiao, L. Ling, D. Long, *Energy Environ. Sci.* **2016**, *9*, 3230.

Manuscript received: May 22, 2019
Revised manuscript received: June 24, 2019
Accepted manuscript online: June 24, 2019
Version of record online: July 25, 2019

© 2019 Wiley-VCH Verlag GmbH & Co. KGaA, Weinheim